To be published in Applied Optics:

Title: (TBO) Gaussian approximations of fluorescence microscope PSF models
Authors: Bo Zhang, Josiane Zerubia, and Jean-Christophe Olivo-Marin
Accepted: 15 September 2006
Posted: 21 September 2006
Doc. ID: 71625

Gaussian approximations of fluorescence microscope PSF models

Bo Zhang[ab], Josiane Zerubia[c] and Jean-Christophe Olivo-Marin[a]

[a] *Unité d'Analyse d'Images Quantitative, Institut Pasteur*

25-28 rue du Docteur Roux, 75724 Paris Cedex 15, France

[b] *Ecole Nationale Supérieure des Télécommunications*

46 rue Barrault, 75013 Paris, France

[c] *Ariana Project (INRIA/I3S) Institut National de Recherche en Informatique et en Automatique*

2004 route des lucioles - BP 93, 06902 Sophia-Antipolis Cedex, France

{bzhang,jcolivo}@pasteur.fr, josiane.zerubia@inria.fr

This paper studies comprehensively the least squares Gaussian approximations of the diffraction-limited 2D/3D paraxial/non-paraxial point spread functions (PSFs) of Wide Field Fluorescence Microscope (WFFM), Laser Scanning Confocal Microscope (LSCM) and Disk Scanning Confocal Microscope (DSCM). The PSFs are expressed using the Debye integral. Under an L^∞ constraint imposing peak matching, optimal and near-optimal Gaussian parameters are derived for the PSFs. With an L^1 constraint imposing energy conservation, an optimal Gaussian parameter is derived for the 2D paraxial WFFM PSF. We found that: (i) the 2D approximations are all very accurate; (ii) no accurate Gaussian approximation exists for 3D WFFM PSFs; (iii) with typical pinhole sizes, the 3D approximations are accurate for DSCM and nearly perfect for LSCM. All the Gaussian parameters derived in this study are in explicit analytical forms, allowing their direct use in practical applications.

OCIS codes: 999.9999 (point spread function), 000.4430, 180.2520, 180.1790, 180.6900, 110.0180.

1. Introduction

The PSFs of fluorescence microscopes, e.g. Wide Field Fluorescence Microscope (WFFM), Laser Scanning Confocal Microscope (LSCM) and Disk Scanning Confocal Microscope (DSCM), play a central role in understanding the imaging performances, such as the theoretical resolution limit and the optical sectioning capacity. A great amount of research has focused on deriving more and more accurate PSF models based on wave optics (cf. Ref. 1

and the cited references in it). Despite the availability of these rigorous physical models of PSFs, approximative PSFs and particularly separable Gaussian approximations are widely preferred in practical microscopic applications requiring fast data processing, such as single fluorescent particle tracking,[2–4] fluorescent dot localization and tracking with super-resolution,[5,6] and myopic deconvolution.[7] Indeed, compared with a physical PSF model, which usually involves non-trivial terms such as integrals and infinite series, a Gaussian approximative PSF is much simpler and can be computed much faster. Furthermore, due to its special analytical form and nice properties (semi-group property, invariance under Fourier transform, etc.), a Gaussian PSF is often chosen to facilitate theoretical analysis and modeling, such as the derivation of analytical solutions to 3D Fluorescence Recovery After Photobleaching (FRAP) process,[8,9] the modeling of 3D tubular structures in confocal images[10] and the analysis of convergence properties of EM deconvolution.[11]

Despite the popularity of Gaussian approximations, most of the above mentioned works either assume the validity of the approximations or only justify them empirically on observed data. The approximation accuracy and the selection of Gaussian parameters have rarely been rigorously investigated with any physical PSF model, leaving these approximations essentially arbitrary. To the best of our knowledge, only a few works[6,12] considered the approximations based on physical models, but they solely covered the paraxial WFFM PSF case with an L^∞ constraint (see section 3 for details on this constraint).

This paper, which extends and generalizes our previous work,[13] studies comprehensively the least squares Gaussian approximations of the diffraction-limited 2D/3D paraxial/non-paraxial PSFs of WFFM, LSCM and DSCM. The PSFs are expressed using the Debye integral, presented in section 2. Then, in section 3 we derive, under an L^∞ constraint imposing peak matching, optimal and near-optimal Gaussian parameters for the WFFM, LSCM and DSCM PSFs. Next, we consider in section 4 the approximations with an L^1 constraint imposing energy conservation, where an optimal Gaussian parameter is derived for the 2D paraxial WFFM PSF. Numerical results in section 5 show that: (i) the 2D approximations are all very accurate; (ii) no accurate Gaussian approximation exists for 3D WFFM PSFs; (iii) with typical pinhole sizes, the 3D approximations are accurate for DSCM and nearly perfect for LSCM. All the Gaussian parameters derived in this work are in explicit analytical forms and are listed in Tables 1, 2 and 3. We conclude in section 6 and defer the mathematical details to appendices.

2. Theoretical diffraction-limited PSF models

In this work, the PSF models are supposed to be diffraction-limited and aberrations will be ignored. Our models are based on the Debye diffraction integral, presented below.

2.A. Paraxial and non-paraxial Debye integrals

Consider a uniformly illuminated microscope objective lens. The illumination wave of vacuum wavelength λ is transformed into a converging spherical wave propagating in the object space, which has a refractive index n and a wavenumber $k = n\frac{2\pi}{\lambda}$. This situation is presented in Figure 1, where we also show the coordinate system used in this paper. Then, the near-focus amplitude distribution $\mathbf{h}$ can be expressed by the scalar Debye diffraction integral:[1]

$$\mathbf{h}(x, y, z; \lambda) = C_0 \int_0^\alpha \sqrt{\cos\theta}\, J_0(k\rho \sin\theta) e^{-ikz\cos\theta} \sin\theta \, d\theta \tag{1}$$

where C_0 is a complex constant, J_0 is the zero-order Bessel function of the first kind, $\rho = \sqrt{x^2 + y^2}$ and α is the maximal convergence semi-angle of the objective. The apodization term $\sqrt{\cos\theta}$ in (1) results from the sine condition[1, 14] verified by aplanatic lenses as generally used on commercial microscopes. It is known that the Debye model is well adapted to approximate the near-focus light distribution in non-paraxial imaging, i.e. when a high NA (Numerical Aperture) objective is employed.[1]

Now, if we decrease the value of NA, it can be seen that (1) tends asymptotically to the following paraxial model ($\sin\theta \approx \theta$),[1, 14]

$$\mathbf{h}(x, y, z; \lambda) = C_1 e^{-ikz} \int_0^1 J_0(k\rho t \sin\alpha) e^{\frac{i}{2}kzt^2 \sin^2\alpha} t\, dt \tag{2}$$

where $C_1 = \alpha^2 C_0$. In both paraxial and non-paraxial cases, the intensity distribution is given by $|\mathbf{h}|^2$.

2.B. PSF models of WFFM, LSCM and DSCM

We suppose that the pinholes in LSCM and DSCM are circular with a radius $r = D/2$ in the object space, and that the emission fluorescence is incoherent. To derive the object-space PSFs[15] of WFFM, LSCM and DSCM, we will make use of the Helmholtz reciprocity theorem.[16] As a direct result of this theorem, the intensity PSF of WFFM is given by

$$\mathrm{PSF}_{WFFM}(x, y, z) = |\mathbf{h}(x, y, z; \lambda_{em})|^2 \tag{3}$$

where λ_{em} is the fluorescence emission wavelength.

Using the property of the near-linear dynamics of fluorescence emission under usual laser excitation[17] and the reciprocity theorem, the LSCM PSF is the product of excitation and emission intensity distributions:

$$\mathrm{PSF}_{LSCM}(x,y,z) = |\mathbf{h}(x,y,z;\lambda_{ex})|^2 \cdot \int_{\{x_1^2+y_1^2\leq r^2\}} |\mathbf{h}(x-x_1,y-y_1,z;\lambda_{em})|^2\, dx_1 dy_1 \quad (4)$$

where λ_{ex} denotes the laser excitation wavelength.

To derive the DSCM PSF, we use the fact that the pinholes on the disk of DSCM form a nearly periodic hexagonal pattern in the object space[18,19] with an adjacent pinhole distance d. Then, the DSCM PSF is given by[19]

$$\begin{aligned}\mathrm{PSF}_{DSCM}(x,y,z) &= \left|\sum_{(n_x,n_y)\in\mathcal{D}} \mathbf{h}\left(x-\frac{d}{2}(n_x+n_y), y-\frac{\sqrt{3}}{2}d(n_x-n_y), z;\lambda_{ex}\right)\right|^2 \cdot \\ &\quad \int_{\{x_1^2+y_1^2\leq r^2\}} |\mathbf{h}(x-x_1,y-y_1,z;\lambda_{em})|^2\, dx_1 dy_1 \qquad (5)\end{aligned}$$

where the total excitation distribution is the sum of the individual excitation distributions from the illuminating pinholes whose index set is denoted as $\mathcal{D} \subset \mathbf{Z}^2$. We point out that, in this paper, the light source of DSCM is assumed to be a laser, since it is the most widely used source in commercial microscopes. Thus, as a coherent source is used, the first modulus sign in (5) is applied to the entire sum instead of to each summing term.

Finally, the expressions of the paraxial PSFs of the three microscopes are obtained by inserting the paraxial integral (2) into (3), (4) and (5). The expressions of the non-paraxial PSFs are derived likewise except that the non-paraxial integral (1) should be used. It can be verified from these expressions that all the PSFs have mirror symmetry about the xy-plane. Furthermore, PSF_{WFFM} and PSF_{LSCM} have circular symmetry about the z-axis, and PSF_{DSCM} is almost circularly symmetric if the distance d is sufficiently large.

3. Gaussian approximations of the PSF models with an L^∞ constraint

To derive Gaussian approximations of the PSFs given in (3), (4) and (5), we suppose in the following that the Gaussian functions are centered at the origin of the PSFs and are separable. We make these two assumptions not only because they simplify the calculus and are widely adopted as stated before, but also because centered separable Gaussians are the only Gaussian functions that preserve the intrinsic symmetries in the PSF models (cf. Proposition A.1, Appendix A). Therefore, the 2D and 3D Gaussians g_σ are respectively given by:

$$g_{\sigma_\rho}(x,y) := A_1 \exp\left(-\frac{x^2+y^2}{2\sigma_\rho^2}\right) = A_1 \exp\left(-\frac{\rho^2}{2\sigma_\rho^2}\right) \quad (6)$$

$$g_{\sigma_\rho,\sigma_z}(x,y,z) := A_2 \exp\left(-\frac{x^2+y^2}{2\sigma_\rho^2} - \frac{z^2}{2\sigma_z^2}\right) = A_2 \exp\left(-\frac{\rho^2}{2\sigma_\rho^2} - \frac{z^2}{2\sigma_z^2}\right) \quad (7)$$

We want to find the best Gaussian parameter, i.e. $\sigma^* = \sigma_\rho^*$ in 2D and $\sigma^* = \{\sigma_\rho^*, \sigma_z^*\}$ in 3D, that minimizes the least squares (LSQ) criterion, i.e.

$$\sigma^* = \underset{\sigma>0}{\operatorname{argmin}} \|\mathrm{PSF} - g_\sigma\|_2^2 \quad (8)$$

In this section, we suppose that the Gaussian functions and the PSFs are normalized according to their L^∞ norm i.e. $\|g_\sigma\|_\infty = \|\mathrm{PSF}\|_\infty = 1$. We have thus $A_1 = A_2 = 1$. It can be noted that since the Gaussians, the WFFM PSFs, the LSCM PSFs and the DSCM PSFs (with d sufficiently large) are all maximized at the origin, this normalization imposes matching the peaks of g_σ and the PSF. In the following, we will denote by $\hat{\sigma}^*$ the proposed parameter and by σ^* the optimal parameter given by (8).

3.A. Gaussian approximations of 2D WFFM PSFs

We begin with the 2D paraxial WFFM PSF, which is known as "Airy disk" and can be directly derived from (2) and (3) by setting $z = 0$, i.e.

$$\mathrm{PSF}_{WFFM}(\rho) = \left[2\frac{J_1(k_{em}\mathrm{NA}\rho)}{k_{em}\mathrm{NA}\rho}\right]^2 \tag{9}$$

where J_1 is the first order Bessel function of the first kind and $k_{em} = \frac{2\pi}{\lambda_{em}}$ is the emission wavenumber. Proposition B.2 (cf. Appendix B) shows that the solution to (8) is

$$\sigma_\rho^* \approx 0.21\frac{\lambda_{em}}{\mathrm{NA}} \tag{10}$$

This value was first given in Ref. 6, and a complete proof can be found in Ref. 13.

Unlike the paraxial case where the optimal parameter value can be found exactly, a direct minimization of (8) is difficult in the non-paraxial case since the non-paraxial PSF, derived by inserting (1) into (3) with $z = 0$, has no closed form. However, we can note that the L^2 energy of the PSF ($\|\mathrm{PSF}_{WFFM}\|_2^2$) concentrates mostly in the main lobe, which is situated in a small neighborhood of the origin. Therefore, an approximation near the origin capturing the decay of the main lobe, e.g. $g_\sigma(\rho) \to \mathrm{PSF}_{WFFM}(\rho)$ as $\rho \to 0$, can be expected to give a good global approximation. This can be easily achieved by matching the Maclaurin series of the PSF (29) with that of a Gaussian function (27) with $z = 0$. The two expansions differ in their second and higher order terms. Thus, by imposing the equality on their second order terms, we obtain:

$$\hat{\sigma}_\rho^* = \frac{1}{nk_{em}}\left[\frac{4 - 7\cos^{\frac{3}{2}}\alpha + 3\cos^{\frac{7}{2}}\alpha}{7(1-\cos^{\frac{3}{2}}\alpha)}\right]^{-\frac{1}{2}} \tag{11}$$

The positivity of the bracketed term in (11) can be easily verified, so $\hat{\sigma}_\rho^*$ is well defined. From a geometric point of view, this approach matches the principal curvatures of the graphs of the two functions at the origin,[12] since the gradients and the second-order mixed derivatives of the PSF and of the Gaussian vanish at the origin.

The near-optimality of (11) under the original LSQ criterion (8) will be confirmed by the numerical results in section 5. Yet, the consistency analysis below already sheds some light on why (11) can be considered as a "good" parameter.

3.A.1. Consistency of the Gaussian parameters

As $\alpha \to 0$ or $\mathrm{NA} \to 0$, i.e. as the system becomes paraxial, we have,

$$\lim_{\alpha \to 0+} \frac{(11)}{\sqrt{2}/(k_{em}\mathrm{NA})} = 1 \tag{12}$$

Therefore, (11) tends asymptotically to $\sqrt{2}/(k_{em}\mathrm{NA}) \approx 0.225\lambda_{em}/\mathrm{NA}$, a value only a few percent larger than (10). This implies that the non-paraxial parameter (11) gets close to the optimal solution in the paraxial limit.

3.B. Gaussian approximations of 2D LSCM PSFs

The Maclaurin expansion of the 2D paraxial LSCM PSF is given by (30) with $z = 0$. By applying the same series-matching method as in section 3.A, the Gaussian parameter is found to be:

$$\hat{\sigma}_\rho^* = \sqrt{2}\left[\frac{c_1^2}{r^2} + \frac{4c_2 J_0(c_2)J_1(c_2) - 8J_1^2(c_2)}{r^2[J_0^2(c_2) + J_1^2(c_2) - 1]}\right]^{-\frac{1}{2}} \tag{13}$$

where $c_1 = k_{ex}r\mathrm{NA}$, $c_2 = k_{em}r\mathrm{NA}$ and $k_{ex} = \frac{2\pi}{\lambda_{ex}}$ is the excitation wavenumber.

In the non-paraxial case, due to the complexity of the non-paraxial PSF, the parameter derived by series matching has no closed-form expression, which is inconvenient for practical use. One solution to this is based on the observation that the non-paraxial LSCM PSF will be much simplified if the terms $|\mathbf{h}|$ in (4) are first approximated by Gaussian functions. This pre-approximation of the PSF model is reasonable, since the terms $|\mathbf{h}|$ share the same form as the 2D non-paraxial WFFM PSF, which can be very accurately approximated by the Gaussians with the parameters derived in the previous section (see section 5 for the numerical results). By matching the series of this pre-approximated PSF, i.e. (31) with $z = 0$, and that of a Gaussian, we obtain:

$$\hat{\sigma}_\rho^* = \sqrt{2}\left[\frac{2\sigma_{em,\rho}^4\left[\exp\left(\frac{r^2}{2\sigma_{em,\rho}^2}\right)-1\right]+r^2\sigma_{ex,\rho}^2}{\sigma_{ex,\rho}^2\sigma_{em,\rho}^4\left[\exp\left(\frac{r^2}{2\sigma_{em,\rho}^2}\right)-1\right]}\right]^{-\frac{1}{2}} \tag{14}$$

where $\sigma_{em,\rho}$ is given by (11) and $\sigma_{ex,\rho}$ is also expressed by (11) with k_{em} replaced by k_{ex}.

3.B.1. Consistency of the Gaussian parameters

First, we can see that as the system becomes paraxial, the non-paraxial parameter (14) tends asymptotically to the paraxial one (13):

$$\lim_{\alpha\to 0+}\frac{(14)}{(13)} = 1 \tag{15}$$

Second, we study the asymptotic behavior of (13) and (14) in the vanishing pinhole case ($r \to 0+$), i.e. as the system approaches ideal confocality. In this situation, the pinhole is modelled as a Dirac distribution and the LSCM PSF (4) simply reduces to the product of two WFFM PSFs. Maclaurin series matching is then applied for this ideal confocality case to derive the paraxial and non-paraxial Gaussian parameters, given by (16) and (17) respectively.

$$\hat{\sigma}_\rho^* = \frac{\sqrt{2}}{2\pi\mathrm{NA}}\frac{\lambda_{ex}\lambda_{em}}{(\lambda_{ex}^2+\lambda_{em}^2)^{1/2}} \tag{16}$$

$$\hat{\sigma}_\rho^* = \frac{\lambda_{ex}\lambda_{em}}{2\pi n(\lambda_{ex}^2+\lambda_{em}^2)^{\frac{1}{2}}}\left[\frac{7\cos^{\frac{3}{2}}\alpha - 3\cos^{\frac{7}{2}}\alpha - 4}{7(\cos^{\frac{3}{2}}\alpha - 1)}\right]^{-\frac{1}{2}} \tag{17}$$

The following results confirm the consistency of the parameters (13) and (14) with (16) and (17) as $r \to 0+$.

$$\lim_{r \to 0+} (13) = (16), \quad \lim_{r \to 0+} (14) = (17) \tag{18}$$

Interestingly, we can note that if the Stokes shift[17] is negligible, i.e. $\lambda_{ex} \approx \lambda_{em}$, both pairs of equations (10)(16) and (11)(17) imply that in the ideal confocality situation, the effective width of the LSCM PSF is approximately 1.4 times smaller than that of the WFFM PSF. Here, we see the well-known resolution gain factor in LSCM.

Finally, for a full-open pinhole ($r \to +\infty$), the equations below show that the Gaussian parameters (13) and (14) tend towards those of WFFM with λ_{em} replaced by λ_{ex}, which is consistent with the known fact that in this case an LSCM behaves as a WFFM.

$$\lim_{r \to +\infty} (13) = \frac{\sqrt{2}}{k_{ex}\mathrm{NA}} \approx 0.225 \frac{\lambda_{ex}}{\mathrm{NA}}, \quad \lim_{r \to +\infty} (14) = \frac{1}{nk_{ex}} \left[\frac{7\cos^{\frac{3}{2}}\alpha - 3\cos^{\frac{7}{2}}\alpha - 4}{7(\cos^{\frac{3}{2}}\alpha - 1)} \right]^{-\frac{1}{2}} \tag{19}$$

3.C. Gaussian approximations of 2D DSCM PSFs

The DSCM case is more complex as the approximation quality varies with the adjacent pinhole distance d. We will assume that d is sufficiently large so that the PSF is almost circularly symmetric, or equivalently, that the contribution of individual excitation distributions from adjacent pinholes to the total PSF is negligible. This condition can be considered fulfilled if the support of the main lobe of the emission PSF contains only one main lobe of the excitation PSF. In terms of d, we should require:

$$d \geq d_0 := \frac{1}{2} \left(\frac{\lambda_{em}}{\lambda_{ex}} + D + 1 \right) \ \mathrm{AU} \tag{20}$$

where "AU" stands for the "Airy Unit", i.e. $1\mathrm{AU} = 1.22 \cdot \lambda_{ex}/\mathrm{NA}$. Under this condition, the DSCM PSF approaches reasonably well the LSCM PSF, and the Gaussian parameters

(13) and (14) can be applied respectively to the paraxial and non-paraxial DSCM PSFs (see also section 5 and Ref. 13).

3.D. Gaussian approximations of 3D PSFs

The Maclaurin series of the 3D paraxial WFFM PSF, 3D non-paraxial WFFM PSF, 3D paraxial LSCM PSF and 3D pre-approximated non-paraxial LSCM PSF are given by (28), (29), (30) and (31). The lateral and axial Gaussian parameters for these PSFs are found by the same series matching method as described in the 2D case. The same Gaussian parameters as LSCM are proposed for the DSCM PSFs under the condition (20).

Tables 1, 2 and 3 summarize the proposed 2D and 3D Gaussian parameters. The consistency of the 3D parameters can be studied in the same manner as in the 2D case and the main results are listed below:

Paraxial system: As the NA becomes small, the 3D non-paraxial lateral and axial Gaussian parameters of WFFM, LSCM and DSCM tend asymptotically to the paraxial Gaussian parameters;

Ideal confocality: As the pinhole radius approaches zero, the 3D lateral and axial Gaussian parameters of LSCM and DSCM converge to the parameters derived in the vanishing pinhole situation;

Full-open pinhole: As the pinhole radius tends to infinity, the 3D Gaussian parameters of LSCM and DSCM approach those of WFFM with λ_{em} replaced by λ_{ex}, *except for* the non-paraxial axial parameter $\hat{\sigma}_z^*$. The latter exception implies that the 3D non-paraxial Gaussian approximations of LSCM and DSCM PSFs cannot be applied to large pinhole situations.

4. Gaussian approximations of the PSF models with an L^1 constraint

In the applications where photometry should be preserved, it is important to consider the L^1 constraint $\|g_\sigma\|_1 = \|\mathrm{PSF}\|_1 = 1$ in the optimization problem (8) instead of the L^∞ constraint. This constraint requires the PSF energy to be conserved by the Gaussian function used to approximate the PSF.

Note that this constrained optimization is infeasible for 3D WFFM PSFs, since they are not L^1 functions. In general, analytical solutions to this optimization problem are difficult to obtain except for the 2D paraxial WFFM case, where we can show (cf. Proposition B.2, Appendix B):

$$\sigma_\rho^* \approx 0.22 \frac{\lambda_{em}}{\mathrm{NA}} \tag{21}$$

We point out that the general result of the approximation of the 2D paraxial WFFM PSF with an L^p constraint ($1 \leq p \leq \infty$) is presented in Proposition B.3 (cf. Appendix B).

5. Numerical evaluations of the approximations

The approximation error is evaluated using the Relative Squared Error (RSE) defined by

$$\mathrm{RSE} := \frac{\|\mathrm{PSF} - g_{\hat{\sigma}^*}\|_2^2}{\|\mathrm{PSF}\|_2^2} \tag{22}$$

where the Gaussian function and the PSF are both normalized according to their L^∞ norm or L^1 norm, depending on the approximation constraint used. Clearly, this criterion is essentially the same as the one defined in (8), since the squared L^2 norm of the PSF in (22) is just a normalizing constant. To compute the optimal Gaussian parameter σ^* of (8), a numerical LSQ fit is used. Then, the Parameter Relative Error (PRE), i.e. $|\hat{\sigma}^* - \sigma^*|/\sigma^*$, is evaluated.

5.A. *Numerical results*

In our simulations, λ_{ex} and λ_{em} are set to 488nm and 520nm respectively, which are two wavelengths frequently used in real experiments. The refractive index is set to $n = 1.515$, which is the typical value of immersion oils. In LSCM and DSCM, the pinhole diameter ranges from 0AU to 3AU, i.e. from a vanishing size to a large size. For DSCM, d is set to d_0. The NA varies from 0.2 to 0.7 in the paraxial cases, and from 0.8 to 1.4 in the non-paraxial cases. Given an NA value, the exact theoretical PSFs are computed using (3), (4) and (5), the Gaussian approximations are generated using the parameters shown in Tables 1, 2 and 3, and then the approximation errors are evaluated. The results of the approximations with the L^∞ constraint are shown in Tables 4, 5 and 6, where we present the minimal and maximal RSE values for the WFFM, LSCM and DSCM cases. The minimal and maximal PRE values of the lateral and axial parameters ($\hat{\sigma}^*_\rho$ and $\hat{\sigma}^*_z$) are also shown. The results of the approximation of the 2D paraxial WFFM PSF with the L^1 constraint are given in Table 7. Examples of the Gaussian approximations with the two constraints are presented in Fig. 2 and Fig. 3.

5.B. *Discussion*

The following conclusions can be drawn by examining Tables 4, 5, 6 and 7.

2D approximations for WFFM, LSCM and DSCM The approximation accuracy for all 2D PSFs is very high, since we have RSE $< 2\%$ in WFFM (cf. Tables 4 and 7), $\leq 2\%$ in LSCM (cf. Table 5) and $< 4\%$ in DSCM (cf. Table 6).

3D approximations for WFFM Table 4 shows that the approximations of the 3D WFFM PSFs are only average, as an RSE of about 17% is observed. However, this is not a defect of the Maclaurin series matching method, since the very low PRE values ($\simeq 2\%$) confirm the near-optimality of the proposed parameter $\hat{\sigma}^*$. Indeed, the numerical LSQ Gaussian fits are found to result in almost the same RSE (data not shown). It follows that an RSE of about 17% is the lower error bound, whatever the approximation approach used. This inaccuracy is actually due to the fact that the axial WFFM PSF decreases slowly (as $O(z^{-2})$). In contrast, the axial decreasing speed of the LSCM PSF with typical pinhole sizes is much higher (as $O(z^{-4})$), since the PSF is in the form of the product of excitation and emission PSFs both having $O(z^{-2})$ as decreasing rate. This can also be seen in Figure 2, where secondary lobes with significant amplitudes are present in Figure 2(d) (axial WFFM PSF), while they are almost invisible in Figure 2(e) (axial LSCM PSF). Hence, Gaussian approximations perform much better for LSCM with typical pinhole sizes (see below).

3D approximations for LSCM and DSCM Tables 5 and 6 show that, the 3D approximations are accurate for DSCM with typical pinhole sizes (RSE $< 7\%$, $D < 1$AU), and accurate for LSCM up to reasonably large pinhole sizes (RSE $< 9\%$, $D < 3$AU). In particular, the 3D approximations for LSCM with typical pinhole sizes are nearly perfect (RSE

$< 1\%$, $D < 1\text{AU}$).

As pinholes become larger and larger, the PSFs tend asymptotically to WFFM PSFs. It follows from the previous discussion on 3D approximations for WFFM that in this case, any Gaussian approximation will become inaccurate. In the experiments, as can be seen in Table 5, the performance of our approximations for LSCM degrades (RSE $> 10\%$) as $D \geq 3\text{AU}$. In the case of DSCM, the RSE values are larger than 10% as long as $D \geq 1\text{AU}$ (cf. Table 6).

Therefore, we conclude that the regions where our 3D approximations perform accurately for LSCM and for DSCM are given by the sets of D satisfying $D < 3\text{AU}$ and $D < 1\text{AU}$, respectively.

Accuracy of Gaussian parameters As can be seen from Tables 4, 5 and 7, in the cases of WFFM, 2D LSCM, and 3D LSCM with $D < 3\text{AU}$, almost all the PRE values are within only a few percent, implying the near-optimality of the proposed Gaussian parameters. For 2D DSCM and for 3D DSCM with $D < 1\text{AU}$, the PRE values are generally larger than those in LSCM under the same condition but remain satisfactory (cf. Table 6).

Finally, we point out that as the optimal Gaussian parameters (10) and (21) derived for 2D paraxial WFFM PSF have undergone numerical approximations (see Proposition B.2, Appendix B), their PRE values deviate slightly from zero (cf. Tables 4 and 7).

6. Conclusion

We have studied comprehensively the least squares Gaussian approximations of the diffraction-limited 2D/3D paraxial/non-paraxial PSFs of WFFM, LSCM and DSCM described using the Debye integral. Optimal Gaussian parameters are derived for the 2D paraxial WFFM PSF, under both the L^∞ constraint imposing peak matching and the L^1 constraint imposing energy conservation. For the other PSFs, with the L^∞ constraint, near-optimal parameters in explicit forms are derived using Maclaurin series matching. We found that: (i) the 2D approximations are all very accurate; (ii) no accurate Gaussian approximation exists for 3D WFFM PSFs; (iii) with typical pinhole sizes, the 3D approximations are accurate for DSCM and nearly perfect for LSCM.

This study can be extended along several lines, including approximations of the PSFs described using vectorial Debye integral[1] with various laser polarization modes, and approximations in presence of aberrations.

Appendix A: Gaussian function under the assumption of symmetries

The following proposition was proven in Ref. 13.

Proposition A.1 *(Ref. 13) Assuming a 3D Gaussian distribution*

$$g_\Sigma(\mathbf{x}) := (2\pi)^{-\frac{3}{2}}|\Sigma|^{-\frac{1}{2}} \exp\left(-\frac{1}{2}(\mathbf{x}-\boldsymbol{\mu})^T\Sigma^{-1}(\mathbf{x}-\boldsymbol{\mu})\right)$$

where we denote $\mathbf{x} = (x, y, z)^T$*, the mean vector* $\boldsymbol{\mu} = (\mu_x, \mu_y, \mu_z)^T$ *and the covariance matrix* $\Sigma = [\sigma_{ij}]_{1\le i,j\le 3}$*.* g_Σ *has circular symmetry about the z-axis and mirror symmetry about the xy-plane if and only if* $\mu = \mathbf{0}$ *and* Σ *is diagonal with* $\sigma_{11} = \sigma_{22}$*.*

Appendix B: Optimal Gaussian parameter for the 2D paraxial WFFM PSF

We recall the expressions of the Airy function h and the Gaussian function g_σ:

$$h(\rho) = \left(2\frac{J_1(c\rho)}{c\rho}\right)^2 \quad \text{and} \quad g_\sigma(\rho) = \exp\left(-\frac{\rho^2}{2\sigma^2}\right)$$

where $c = k_{em}\mathrm{NA}$. We define the objective function for $1 \leq p \leq \infty$,

$$E_p(\sigma) := \left\| \frac{h}{\|h\|_p} - \frac{g_\sigma}{\|g_\sigma\|_p} \right\|_2^2$$

In the following, I_n denotes the n-th order modified Bessel functions of the first kind.

Proposition B.2 *The unique solutions to* $\operatorname{argmin}_{\sigma>0} E_p(\sigma)$ *for* $p = 1$ *and* $p = \infty$ *are:*

$$\sigma^* \approx \begin{cases} 0.22\lambda_{em}/NA & p = 1 \\ 0.21\lambda_{em}/NA & p = \infty \end{cases} \tag{23}$$

Proof: In the following, we will prove the case $p = 1$. The proof of the case $p = \infty$ is completely similar and is provided in Ref. 13.

As $\|h\|_1 = \frac{4\pi}{c^2}$ (cf. Ref. 20), we have (the calculus details are in the proof of Proposition B.3):

$$\frac{\partial E_1}{\partial \sigma}(\sigma) = \frac{3e^{c^2\sigma^2} - 4I_0(c^2\sigma^2) - 8I_1(c^2\sigma^2)}{2\pi\sigma^3 e^{c^2\sigma^2}} \tag{24}$$

We define the numerator of (24) as $f(u) := 3e^u - 4I_0(u) - 8I_1(u)$ where $u = c^2\sigma^2$. Then we have, on one hand, $f(u) < 0$ in a right neighborhood of the origin; on the other hand, $f(u) \to +\infty$ as $u \to +\infty$. Therefore, there must exist at least one u^* such that $f(u^*) = 0$.

We will prove the uniqueness of u^*. The series expansion of $f''(u)$ is given by:

$$\begin{aligned} f''(u) &= 1 + \sum_{k=1}^{\infty} (k+1)(k+2)c_k \cdot u^k \\ c_k &= \begin{cases} \frac{3}{(2n)!} - \frac{4}{2^{2n}(n!)^2} & k = 2n-2 \\ \frac{3}{(2n+1)!} - \frac{4}{2^{2n}n!(n+1)!} & k = 2n-1 \end{cases} \qquad n = 1, 2, \ldots \end{aligned}$$

It can be shown from induction that $c_k \geq 0$, so $f''(u) > 0$ for $u \geq 0$. This strict convexity of f on $[0, +\infty)$ together with the fact that $f(0) = -1 < 0$ ensures the uniqueness of u^*.

We have thus $f(u) < 0$ on $(0, u^*)$ and $f(u) > 0$ on $(u^*, +\infty)$. Numerically, $u^* \approx 1.9116$. The proof is completed by noting the positivity of the denominator of equation (24). □

The following proposition studies the case of a general value of p.

Proposition B.3 *The solution to* $\operatorname{argmin}_{\sigma>0} E_p(\sigma)$ *for* $1 \leq p \leq \infty$*, if it exists, satisfies necessarily the following equation (taking the limit for the case* $p = \infty$*):*

$$c^2 \|h\|_p \left(\frac{p}{2\pi}\right)^{\frac{1}{p}} \sigma^{2-\frac{2}{p}} \left(1 - \frac{2}{p}\right) = 8\left[p^{-1}\left(e^{-c^2\sigma^2} I_0(c^2\sigma^2) - 1\right) + e^{-c^2\sigma^2} I_1(c^2\sigma^2)(p^{-1}+1)\right] \tag{25}$$

Proof: The case $p = \infty$ is proven in Ref. 13. For $1 \leq p < \infty$, note that $\|g_\sigma\|_p = (2\pi)^{\frac{1}{p}} \sigma^{\frac{2}{p}} p^{-\frac{1}{p}}$, and $\|h\|_p$ is a constant independent of σ. Then, we differentiate the objective function with respect to σ, and for $\sigma > 0$ the differentiate operator and the integral can be shown to be interchangeable:

$$\begin{aligned} \frac{d}{d\sigma} \left\| \frac{h}{\|h\|_p} - \frac{g_\sigma}{\|g_\sigma\|_p} \right\|_2^2 &= 2\pi \int_0^\infty \rho \frac{d}{d\sigma} \left(\frac{h(\rho)}{\|h\|_p} - \frac{g_\sigma(\rho)}{\|g_\sigma\|_p} \right)^2 d\rho \\ &= 4\pi \left(\frac{p}{2\pi}\right)^{\frac{1}{p}} (T_0 + T_1 + T_2) \end{aligned} \tag{26}$$

where

$$\begin{aligned} T_0 &= \left(\frac{p}{2\pi}\right)^{\frac{1}{p}} \sigma^{-\frac{4}{p}-1} \int_0^\infty \exp\left(-\frac{\rho^2}{\sigma^2}\right) \left[\sigma^{-2}\rho^2 - \frac{2}{p}\right] \rho \, d\rho = \left(\frac{p}{2\pi}\right)^{\frac{1}{p}} \frac{p-2}{2p} \sigma^{1-\frac{4}{p}} \\ T_1 &= \frac{8\sigma^{-\frac{2}{p}-1}}{pc^2\|h\|_p} \int_0^\infty J_1^2(c\rho) \exp\left(-\frac{\rho^2}{2\sigma^2}\right) \rho^{-1} \, d\rho = \frac{4\sigma^{-\frac{2}{p}+1}}{p\|h\|_p} \cdot \frac{1 - \exp(-c^2\sigma^2)[I_0(c^2\sigma^2) + I_1(c^2\sigma^2)]}{c^2\sigma^2} \\ T_2 &= -\frac{4\sigma^{-\frac{2}{p}-3}}{\|h\|_p c^2} \int_0^\infty J_1^2(c\rho) \exp\left(-\frac{\rho^2}{2\sigma^2}\right) \rho \, d\rho = -\frac{4\sigma^{-\frac{2}{p}-1}}{\|h\|_p c^2} \exp(-c^2\sigma^2) I_1(c^2\sigma^2) \end{aligned}$$

The results of the integrals T_1 and T_2 are taken from Ref. 20. Finally, the equation (25) is obtained by setting (26) to zero. □

Appendix C: List of Maclaurin Expansions

To simplify the expressions, we define the intensity distributions given by the paraxial and non-paraxial Debye integrals i.e. h_p and h_{np}, and the Gaussian function g_{σ_ρ,σ_z} as follows.

$$\begin{aligned}
h_p(x,y,z;\lambda) &:= \left|\int_0^1 J_0(kt\sqrt{x^2+y^2}\sin\alpha)e^{\frac{i}{2}kzt^2\sin^2\alpha}t\,dt\right|^2 \\
h_{np}(x,y,z;\lambda) &:= \left|\int_0^\alpha \sqrt{\cos\theta}J_0(k\sqrt{x^2+y^2}\sin\theta)e^{-ikz\cos\theta}\sin\theta\,d\theta\right|^2 \\
g_{\sigma_\rho,\sigma_z}(x,y,z) &:= \exp\left(-\frac{x^2+y^2}{2\sigma_\rho^2}-\frac{z^2}{2\sigma_z^2}\right)
\end{aligned}$$

where the wavenumber in the object space $k=n\frac{2\pi}{\lambda}$. The excitation and emission wavenumbers are denoted as $k_{ex}=\frac{2\pi}{\lambda_{ex}}$ and $k_{em}=\frac{2\pi}{\lambda_{em}}$, respectively. We further denote $\mathbf{x}:=(x,y,z)^T$.

Below shows the second-order Maclaurin expansion of the 3D separable Gaussian function:

$$g_{\sigma_\rho,\sigma_z}(x,y,z)=1-\frac{1}{2\sigma_\rho^2}(x^2+y^2)-\frac{1}{2\sigma_z^2}z^2+o(|\mathbf{x}|^2) \quad (27)$$

The expansions of the 3D paraxial and non-paraxial WFFM PSFs are given by:

$$4h_p(x,y,z;\lambda_{em})=1-\frac{k_{em}^2\mathrm{NA}^2}{4}(x^2+y^2)-\frac{k_{em}^2\mathrm{NA}^2\sin^2\alpha}{48}z^2+o(|\mathbf{x}|^2) \quad (28)$$

$$\begin{aligned}
&\frac{9}{4(1-\cos^{\frac{3}{2}}\alpha)^2}h_{np}(x,y,z;\lambda_{em})=1-\frac{n^2k_{em}^2(4-7\cos^{\frac{3}{2}}\alpha+3\cos^{\frac{7}{2}}\alpha)}{14(1-\cos^{\frac{3}{2}}\alpha)}(x^2+y^2) \\
&-\frac{3n^2k_{em}^2\left(4+4\cos^5\alpha-25\cos^{\frac{7}{2}}\alpha+42\cos^{\frac{5}{2}}\alpha-25\cos^{\frac{3}{2}}\alpha\right)}{175(1-\cos^{\frac{3}{2}}\alpha)^2}z^2+o(|\mathbf{x}|^2) \quad (29)
\end{aligned}$$

By denoting $c_1:=k_{ex}r\mathrm{NA}$ and $c_2:=k_{em}r\mathrm{NA}$, the expansion of the 3D paraxial LSCM PSF is given by:

$$\begin{aligned}
&\frac{4k_{em}^2\mathrm{NA}^2}{\pi[1-J_0^2(c_2)-J_1^2(c_2)]}h_p(x,y,z;\lambda_{ex})\int_{t_1^2+t_2^2\le r^2}h_p(x-t_1,y-t_2,z;\lambda_{em})\,dt_1dt_2 \\
&=1-\frac{1}{4}\left[\frac{c_1^2}{r^2}+\frac{4c_2J_0(c_2)J_1(c_2)-8J_1^2(c_2)}{r^2[J_0^2(c_2)+J_1^2(c_2)-1]}\right](x^2+y^2) \\
&-\frac{1}{48}\left[\frac{c_1^2\mathrm{NA}^2}{r^2n^2}-\frac{48c_2^2[J_0^2(c_2)+J_1^2(c_2)]-192J_1^2(c_2)}{n^2k_{em}^2r^4[J_0^2(c_2)+J_1^2(c_2)-1]}\right]z^2+o(|\mathbf{x}|^2) \quad (30)
\end{aligned}$$

If the excitation PSF and the emission PSF are modeled by Gaussian functions $g_{\sigma_{ex,\rho},\sigma_{ex,z}}$ and $g_{\sigma_{em,\rho},\sigma_{em,z}}$, respectively, the expansion of the 3D LSCM PSF is given by:

$$\begin{aligned}
&\frac{\exp\left(\frac{r^2}{2\sigma_{em,\rho}^2}\right)}{2\pi\sigma_{em,\rho}^2\left[\exp\left(\frac{r^2}{2\sigma_{em,\rho}^2}\right)-1\right]} g_{\sigma_{ex,\rho},\sigma_{ex,z}}(x,y,z)\int_{t_1^2+t_2^2\leq r^2} g_{\sigma_{em,\rho},\sigma_{em,z}}(x-t_1,y-t_2,z)\,dt_1dt_2 \\
&= 1-\frac{1}{4}\frac{2\sigma_{em,\rho}^4\left[\exp\left(\frac{r^2}{2\sigma_{em,\rho}^2}\right)-1\right]+r^2\sigma_{ex,\rho}^2}{\sigma_{ex,\rho}^2\sigma_{em,\rho}^4\left[\exp\left(\frac{r^2}{2\sigma_{em,\rho}^2}\right)-1\right]}(x^2+y^2)-\frac{1}{2}\frac{\sigma_{ex,z}^2+\sigma_{em,z}^2}{\sigma_{ex,z}^2\sigma_{em,z}^2}z^2+o(|\mathbf{x}|^2) \quad (31)
\end{aligned}$$

Acknowledgments

The authors would like to thank A.-C. Boccara (ESPCI Paris), F. Chasles (ESPCI Paris), B. Dubertret (ESPCI Paris), R. Heintzmann (King's College London), J. Huang (Stanford Univ.), Z. Kam (Weizmann Institute of Sci.), H. Maître (ENST Paris), J. B. Pawley (Wisconsin-Madison Univ.) and C. Zimmer (Institut Pasteur) for interesting and useful discussions. This project is financed by CNRS, Institut Pasteur and Franco-Israeli P2R program.

References

1. M. Gu, *Advanced Optical Imaging Theory* (Springer-Verlag, Berlin, 2000).
2. C. M. Anderson, G. N. Georgiou, I. E. G. Morrison, G. V. W. Stevenson, and R. J. Cherry, "Tracking of cell surface receptors by fluorescence digital imaging microscopy using a charge-coupled device camera," J. Cell Sci. **101**, 415–425 (1992).
3. G. J. Schütz, H. Schindler, and T. Schmidt, "Single-molecule microscopy on model membranes reveals anomalous diffusion," Biophys. J. **73**, 1073–1080 (1997).
4. M. K. Cheezum, W. F. Walker, and W. H. Guilford, "Quantitative Comparison of Algorithms for Tracking Single Fluorescent Particles," Biophys. J. **81**(4), 2378–2388

(2001).

5. A. Santos and I. T. Young, “Model-based resolution: applying the theory in quantitative microscopy,” Appl. Opt. **39**(17), 2948–2958 (2000).

6. D. Thomann, D. R. Rines, P. K. Sorger, and G. Danuser, “Automatic fluorescent tag detection in 3D with super-resolution: application to the analysis of chromosome movement,” J. Microscopy **208**(1), 49–64 (2002).

7. F. Rooms, W. Philips, and D. S. Lidke, “Simultaneous degradation estimation and restoration of confocal images and performance evaluation by colocalization analysis,” J. Microscopy **218**(1), 22–36 (2005).

8. J. C. G. Blonk, A. Don, H. van Aalst, and J. J. Birmingham, “Fluorescence photobleaching recovery in the confocal scanning light microscope,” J. Microscopy **169**(3), 363–374 (1993).

9. K. Braeckmans, L. Peeters, N. N. Sanders, S. C. D. Smedt, and J. Demeester, “Three-Dimensional Fluorescence Recovery after Photobleaching with the Confocal Scanning Laser Microscope,” Biophys. J. **85**, 2240–2252 (2003).

10. G. J. Streekstra and J. van Pelt, “Analysis of tubular structures in three-dimensional confocal images,” Network: Comput. Neural Syst. **13**, 381–395 (2002).

11. J.-A. Conchello, “Superresolution and convergence properties of the expectation-maximization algorithm for maximum-likelihood deconvolution of incoherent images,” J. Opt. Soc. Am. A **15**(10), 2609–2619 (1998).

12. L. J. van Vliet, “Grey-Scale Measurements in Multi-Dimensional Digitized Images,” Ph.D. thesis, Delft University, The Netherlands (1993).

13. B. Zhang, J. Zerubia, and J.-C. Olivo-Marin, "A study of Gaussian approximations of fluorescence microscopy PSF models," in *Three-Dimensional and Multidimensional Microscopy: Image Acquisition and Processing XIII*, J.-A. Conchello, C. J. Cogswell and T. Wilson, eds., Proc. SPIE **6090**, 60900K (2006).

14. M. Born and E. Wolf, *Principles of Optics*, 7th ed. (Cambridge University Press, 2002).

15. L. Tao and C. Nicholson, "The three-dimensional point spread functions of a microscope objective in image and object space," J. Microscopy **178**(3), 267–271 (1995).

16. L. D. Landau, E. M. Lifshitz, and L. P. Pitaevskii, *Electrodynamics of continuous media* (Pergamon, Oxford, 1984).

17. D. R. Sandison, R. M. Williams, K. S. Wells, J. Strickler, and W. W. Webb, "Quantitative Fluorescence Confocal Laser Scanning Microscopy (CLSM)," in *Handbook of Biological Confocal Microscopy*, J. B. Pawley, ed., 2nd ed. (Plenum, NY, 1995), pp. 39–53.

18. M. Petráň, M. Hadravský, J. Benes, R. Kucera, and A. Boyde, "The tandem scanning reflected light microscope. Part 1 – The principle and its design," in *Proceedings of the Royal Microscopical Society* **20**(3), (Blackwell, UK, 1985), pp. 125–129.

19. J.-A. Conchello and J. W. Lichtman, "Theoretical analysis of a rotating-disk partially confocal scanning microscope," Appl. Opt. **33**(4), 585–596 (1994).

20. I. S. Gradshteyn and I. M. Ryzhik, *Table of Integrals, Series, and Products* (Academic, 1967).

Table 1: Gaussian Parameters for 2D PSFs

Microscope	Gaussian Parameter[1]
Paraxial WFFM (L^∞ constraint)	$\hat{\sigma}_\rho^* = 0.21\lambda_{em}/\text{NA}$
Paraxial WFFM (L^1 constraint)	$\hat{\sigma}_\rho^* = 0.22\lambda_{em}/\text{NA}$
Non-paraxial WFFM (L^∞ constraint)	$\hat{\sigma}_\rho^* = \frac{1}{nk_{em}}\left[\frac{4-7\cos^{\frac{3}{2}}\alpha+3\cos^{\frac{7}{2}}\alpha}{7(1-\cos^{\frac{3}{2}}\alpha)}\right]^{-\frac{1}{2}}$
Paraxial LSCM and DSCM ($d \geq d_0$, L^∞ constraint)	$\hat{\sigma}_\rho^* = \sqrt{2}\left[\frac{c_1^2}{r^2} + \frac{4c_2J_0(c_2)J_1(c_2)-8J_1^2(c_2)}{r^2[J_0^2(c_2)+J_1^2(c_2)-1]}\right]^{-\frac{1}{2}}$
Non-paraxial LSCM and DSCM ($d \geq d_0$, L^∞ constraint)	$\hat{\sigma}_\rho^* = \sqrt{2}\left[\frac{2\sigma_{em,\rho}^4\left[\exp\left(\frac{r^2}{2\sigma_{em,\rho}^2}\right)-1\right]+r^2\sigma_{ex,\rho}^2}{\sigma_{ex,\rho}^2\sigma_{em,\rho}^4\left[\exp\left(\frac{r^2}{2\sigma_{em,\rho}^2}\right)-1\right]}\right]^{-\frac{1}{2}}$

[1] $k_{ex} := \frac{2\pi}{\lambda_{ex}}$, $k_{em} := \frac{2\pi}{\lambda_{em}}$, $c_1 := k_{ex}r\text{NA}$, $c_2 := k_{em}r\text{NA}$, $\sigma_{em,\rho}$ is given by the expression of $\hat{\sigma}_\rho^*$ of the non-paraxial WFFM (L^∞ constraint) and $\sigma_{ex,\rho}$ is given by the same expression with k_{em} replaced by k_{ex}.

Table 2: Lateral Gaussian Parameters for 3D PSFs (L^∞ constraint)

Microscope	Lateral Gaussian Parameter[1]
Paraxial WFFM	$\hat{\sigma}_\rho^* = \sqrt{2}/(k_{em}\mathrm{NA})$
Non-paraxial WFFM	$\hat{\sigma}_\rho^* = \frac{1}{nk_{em}}\left[\frac{4-7\cos^{\frac{3}{2}}\alpha+3\cos^{\frac{7}{2}}\alpha}{7(1-\cos^{\frac{3}{2}}\alpha)}\right]^{-\frac{1}{2}}$
Paraxial LSCM and DSCM ($d \geq d_0$)	$\hat{\sigma}_\rho^* = \sqrt{2}\left[\frac{c_1^2}{r^2} + \frac{4c_2 J_0(c_2)J_1(c_2) - 8J_1^2(c_2)}{r^2[J_0^2(c_2)+J_1^2(c_2)-1]}\right]^{-\frac{1}{2}}$
Non-paraxial LSCM and DSCM ($d \geq d_0$)	$\hat{\sigma}_\rho^* = \sqrt{2}\left[\frac{2\sigma_{em,\rho}^4\left[\exp\left(\frac{r^2}{2\sigma_{em,\rho}^2}\right)-1\right]+r^2\sigma_{ex,\rho}^2}{\sigma_{ex,\rho}^2\sigma_{em,\rho}^4\left[\exp\left(\frac{r^2}{2\sigma_{em,\rho}^2}\right)-1\right]}\right]^{-\frac{1}{2}}$

[1] $k_{ex} := \frac{2\pi}{\lambda_{ex}}$, $k_{em} := \frac{2\pi}{\lambda_{em}}$, $c_1 := k_{ex}r\mathrm{NA}$, $c_2 := k_{em}r\mathrm{NA}$, $\sigma_{em,\rho}$ is given by the expression of $\hat{\sigma}_\rho^*$ of the non-paraxial WFFM and $\sigma_{ex,\rho}$ is given by the same expression with k_{em} replaced by k_{ex}.

Table 3: Axial Gaussian Parameters for 3D PSFs (L^∞ constraint)

Microscope	Axial Gaussian Parameter[1]
Paraxial WFFM	$\hat{\sigma}_z^* = 2\sqrt{6} \cdot n/(k_{em}\mathrm{NA}^2)$
Non-paraxial WFFM	$\hat{\sigma}_z^* = \frac{5\sqrt{7}(1-\cos^{\frac{3}{2}}\alpha)}{\sqrt{6}\cdot nk_{em}\left[4\cos^5\alpha-25\cos^{\frac{7}{2}}\alpha+42\cos^{\frac{5}{2}}\alpha-25\cos^{\frac{3}{2}}\alpha+4\right]^{\frac{1}{2}}}$
Paraxial LSCM and DSCM ($d \geq d_0$)	$\hat{\sigma}_z^* = 2\sqrt{6}\left[\frac{c_1^2\mathrm{NA}^2}{r^2n^2} - \frac{48c_2^2[J_0^2(c_2)+J_1^2(c_2)]-192J_1^2(c_2)}{n^2k_{em}^2r^4[J_0^2(c_2)+J_1^2(c_2)-1]}\right]^{-\frac{1}{2}}$
Non-paraxial LSCM and DSCM ($d \geq d_0$)	$\hat{\sigma}_z^* = \frac{\sigma_{ex,z}\sigma_{em,z}}{\left[\sigma_{ex,z}^2+\sigma_{em,z}^2\right]^{\frac{1}{2}}}$

[1] $k_{ex} := \frac{2\pi}{\lambda_{ex}}$, $k_{em} := \frac{2\pi}{\lambda_{em}}$, $c_1 := k_{ex}r\mathrm{NA}$, $c_2 := k_{em}r\mathrm{NA}$, $\sigma_{em,z}$ is given by the expression of $\hat{\sigma}_z^*$ of the non-paraxial WFFM and $\sigma_{ex,z}$ is given by the same expression with k_{em} replaced by k_{ex}.

Table 4: Approximation Errors[§] on WFFM PSFs (L^∞ constraint)

RSE%	2D Parax.	2D Non-Parax.	3D Parax.		3D Non-Parax.	
	(0.4, 0.5)	(1.6, 1.7)	(16.0, 19.9)		(16.2, 17.4)	
PRE%	$\hat{\sigma}_\rho^*$	$\hat{\sigma}_\rho^*$	$\hat{\sigma}_\rho^*$	$\hat{\sigma}_z^*$	$\hat{\sigma}_\rho^*$	$\hat{\sigma}_z^*$
	(0.3, 1.5)	(7.0, 7.0)	(0.6, 2.0)	(2.1, 2.4)	(2.2, 2.6)	(0.9, 1.9)

[§] The top part of the table shows the RSE% and the bottom part shows the PRE%. In parentheses, the minimal and maximal errors are shown: (Min.Err.%, Max.Err.%). The NA varies from 0.2 to 0.7 in the paraxial cases and from 0.8 to 1.4 in the non-paraxial cases.

Table 5: Approximation Errors[§] on LSCM PSFs (L^{∞} constraint)

RSE%	2D Parax.	2D Non-Parax.	3D Parax.		3D Non-Parax.	
D=0[†]	(0.1, 0.3)	(0.2, 0.3)	(0.3, 0.4)		(0.4, 0.4)	
D=0.25	(0.1, 0.2)	(0.3, 0.6)	(0.3, 0.5)		(0.5, 0.8)	
D=0.5	(0.1, 0.3)	(0.6, 0.6)	(0.4, 0.5)		(0.6, 0.7)	
D=1	(1.3, 2.0)	(1.0, 1.0)	(1.7, 2.2)		(1.5, 1.6)	
D=2	(1.1, 1.6)	(1.5, 1.6)	(5.3, 5.7)		(7.6, 8.5)	
D=3	(1.1, 1.6)	(1.5, 1.7)	(9.2, 9.6)		(11.8, 13.5)	
PRE%	$\hat{\sigma}_\rho^*$	$\hat{\sigma}_\rho^*$	$\hat{\sigma}_\rho^*$	$\hat{\sigma}_z^*$	$\hat{\sigma}_\rho^*$	$\hat{\sigma}_z^*$
D=0	(0.5, 3.1)	(2.8, 3.2)	(0.2, 2.4)	(2.5, 2.9)	(2.1, 2.5)	(2.2, 2.4)
D=0.25	(0.6, 3.0)	(3.7, 5.2)	(0.3, 2.2)	(2.4, 3.3)	(2.9, 4.3)	(1.9, 2.7)
D=0.5	(0.9, 3.1)	(5.2, 5.3)	(0.2, 2.0)	(1.7, 2.1)	(4.1, 4.2)	(0.9, 1.2)
D=1	(7.4, 9.0)	(5.4, 5.7)	(5.6, 7.3)	(0.0, 0.3)	(3.9, 4.1)	(7.6, 8.3)
D=2	(5.9, 7.5)	(6.9, 7.1)	(1.9, 3.5)	(3.7, 4.0)	(3.3, 3.5)	(20.6, 21.2)
D=3	(5.7, 7.2)	(6.8, 6.9)	(1.0, 2.6)	(2.6, 2.8)	(2.4, 2.8)	(24.0, 24.3)

[§] The top part of the table shows the RSE% and the bottom part shows the PRE%. In parentheses, the minimal and maximal errors are shown: (Min.Err.%, Max.Err.%). The NA varies from 0.2 to 0.7 in the paraxial cases and from 0.8 to 1.4 in the non-paraxial cases.

[†] D is the pinhole diameter and its unit is Airy Unit (1AU = $1.22 \cdot \lambda_{ex}$/NA). D=0 corresponds to the vanishing pinhole situation.

Table 6: Approximation Errors[§] on DSCM PSFs (L^∞ constraint)

RSE%	2D Parax.	2D Non-Parax.	3D Parax.		3D Non-Parax.	
D=0[†]	(3.3, 3.3)	(3.2, 3.4)	(6.1, 6.1)		(3.9, 5.5)	
D=0.25	(2.0, 2.1)	(2.2, 2.4)	(2.8, 2.8)		(2.3, 2.9)	
D=0.5	(0.3, 0.4)	(0.5, 0.7)	(2.3, 2.3)		(2.5, 3.3)	
D=1	(1.2, 1.2)	(2.1, 2.8)	(11.6, 11.8)		(16.2, 18.4)	
D=2	(3.8, 3.8)	(3.7, 4.0)	(16.4, 16.9)		(15.5, 16.7)	
D=3	(1.6, 1.7)	(1.6, 2.3)	(19.0, 21.9)		(23.2, 24.5)	
PRE%	$\hat{\sigma}_\rho^*$	$\hat{\sigma}_\rho^*$	$\hat{\sigma}_\rho^*$	$\hat{\sigma}_z^*$	$\hat{\sigma}_\rho^*$	$\hat{\sigma}_z^*$
D=0	(12.6, 12.6)	(12.3, 12.7)	(14.4, 14.4)	(2.3, 2.3)	(13.5, 14.4)	(0.1, 3.4)
D=0.25	(9.7, 10.2)	(10.1, 10.8)	(10.5, 11.0)	(4.8, 4.9)	(10.5, 11.5)	(5.8, 8.2)
D=0.5	(3.1, 3.2)	(4.2, 5.2)	(3.4, 3.5)	(12.8, 13.0)	(4.1, 5.4)	(14.4, 18.9)
D=1	(5.7, 5.8)	(9.0, 10.4)	(5.6, 5.6)	(26.6, 26.6)	(8.8, 10.1)	(32.9, 35.9)
D=2	(12.4, 12.4)	(11.6, 12.0)	(9.1, 9.1)	(7.4, 7.5)	(8.9, 9.3)	(18.7, 21.0)
D=3	(7.1, 7.1)	(6.8, 7.7)	(2.1, 2.1)	(3.4, 3.4)	(1.9, 3.2)	(20.1, 23.4)

[§] The top part of the table shows the RSE% and the bottom part shows the PRE%. In parentheses, the minimal and maximal errors are shown: (Min.Err.%, Max.Err.%). The NA varies from 0.2 to 0.7 in the paraxial cases and from 0.8 to 1.4 in the non-paraxial cases. d is set to d_0.

[†] D is the pinhole diameter and its unit is Airy Unit (1AU = $1.22 \cdot \lambda_{ex}$/NA). D=0 corresponds to the vanishing pinhole situation.

Table 7: Approximation Errors[§] on the 2D Paraxial WFFM PSF (L^1 constraint)

RSE%	PRE% ($\hat{\sigma}_\rho^*$)
(1.1, 1.3)	(0.0, 1.7)

[§] In parentheses, the minimal and maximal errors are shown: (Min.Err.%, Max.Err.%). The NA varies from 0.2 to 0.7.

List of Figure Captions

Fig. 1. Focusing of an illumination wave by an objective lens.

Fig. 2. Examples of the Gaussian approximations of WFFM, LSCM and DSCM PSFs with an L^∞ constraint. Non-paraxial cases, $\lambda_{ex} = 488$nm, $\lambda_{em} = 520$nm, $n = 1.515$, NA $= 1.0$ and the pinhole diameter $D = 0.5$AU in LSCM and DSCM. (a) Lateral WFFM PSF; (b) Lateral LSCM PSF; (c) Lateral DSCM PSF ($d = d_0$); (d) Axial WFFM PSF; (e) Axial LSCM PSF; (f) Axial DSCM PSF ($d = d_0$).

Fig. 3. Examples of the Gaussian approximations of 2D Paraxial WFFM PSF. (a) approximation with an L^∞ constraint; (b) approximation with an L^1 constraint. $\lambda_{em} = 520$nm, $n = 1.515$ and NA $= 0.3$.

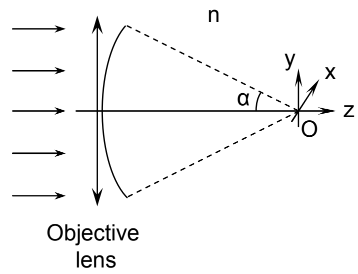

Fig. 1: Focusing of an illumination wave by an objective lens. Zhang_TBO71625_fig1.eps.

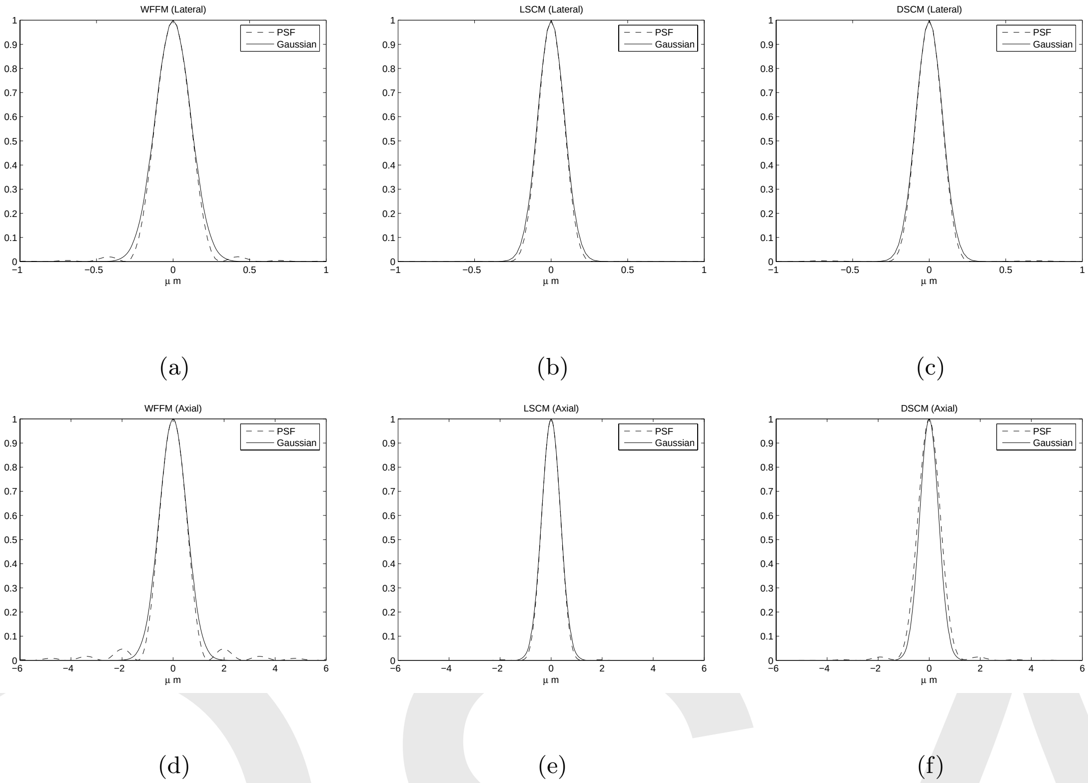

Fig. 2: Examples of the Gaussian approximations of WFFM, LSCM and DSCM PSFs with an L^∞ constraint. Non-paraxial cases, λ_{ex} = 488nm, λ_{em} = 520nm, n = 1.515, NA = 1.0 and the pinhole diameter D = 0.5AU in LSCM and DSCM. (a) Lateral WFFM PSF; (b) Lateral LSCM PSF; (c) Lateral DSCM PSF ($d = d_0$); (d) Axial WFFM PSF; (e) Axial LSCM PSF; (f) Axial DSCM PSF ($d = d_0$). Zhang_TBO71625_fig2.eps.

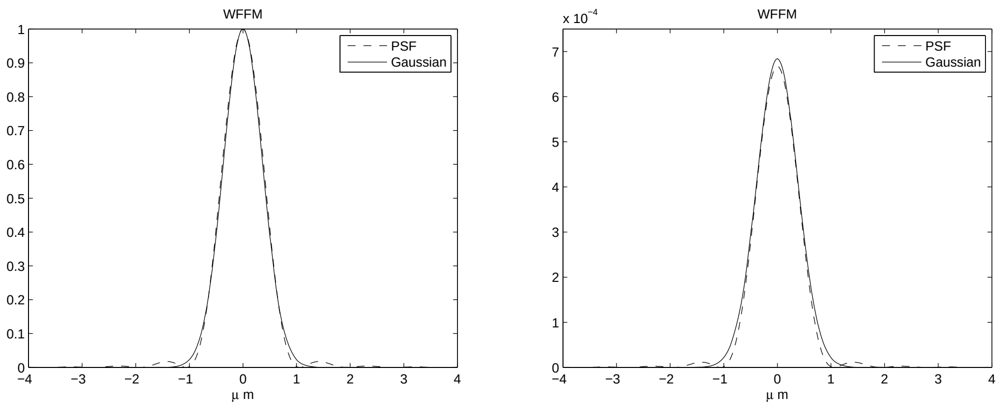

(a) (b)

Fig. 3: Examples of the Gaussian approximations of 2D Paraxial WFFM PSF. (a) approximation with an L^{∞} constraint; (b) approximation with an L^{1} constraint. $\lambda_{em} = 520$nm, $n = 1.515$ and NA $= 0.3$. Zhang_TBO71625_fig3.eps.